

# Spin Susceptibility in Underdoped $\text{YBa}_2\text{Cu}_3\text{O}_{6+x}$

H.F. Fong<sup>1</sup>, P. Bourges<sup>2</sup>, Y. Sidis<sup>2</sup>, L.P. Regnault<sup>3</sup>, J. Bossy<sup>4</sup>, A. Ivanov<sup>5</sup>, D.L. Milius<sup>6</sup>, I.A. Aksay<sup>6</sup>, B. Keimer<sup>1,7</sup>

*1 - Department of Physics, Princeton University, Princeton, NJ 08544 USA*

*2 - Laboratoire Léon Brillouin, CEA-CNRS, CE Saclay, 91191 Gif sur Yvette, France*

*3 - CEA Grenoble, Département de Recherche Fondamentale sur la matière Condensée, 38054 Grenoble cedex 9, France*

*4 - CNRS-CRTBT, BP 166, 38042 Grenoble cedex 9, France*

*5 - Institut Laue-Langevin, 156X, 38042 Grenoble Cedex 9, France*

*6 - Department of Chemical Engineering, Princeton University, Princeton, NJ 08544, USA*

*7 - Max-Planck-Institut für Festkörperforschung, 70569 Stuttgart, Germany*

We report a comprehensive polarized and unpolarized neutron scattering study of the evolution of the dynamical spin susceptibility with temperature and doping in three underdoped single crystals of the  $\text{YBa}_2\text{Cu}_3\text{O}_{6+x}$  high temperature superconductor:  $\text{YBa}_2\text{Cu}_3\text{O}_{6.5}$  ( $T_c = 52$  K),  $\text{YBa}_2\text{Cu}_3\text{O}_{6.7}$  ( $T_c = 67$  K), and  $\text{YBa}_2\text{Cu}_3\text{O}_{6.85}$  ( $T_c = 87$  K). The spin susceptibility is determined in absolute units at excitation energies between 1 and 140 meV and temperatures between 1.5 and 300 K. Polarization analysis is used extensively at low energies. Transitional matrix elements, including those between spin states, in a bilayer system such as  $\text{YBa}_2\text{Cu}_3\text{O}_{6+x}$  can be generally classified into even and odd, according to the sign change under a symmetry operation that exchanges the layers, and both even and odd excitations are detected in  $\text{YBa}_2\text{Cu}_3\text{O}_{6.5}$  and  $\text{YBa}_2\text{Cu}_3\text{O}_{6.7}$ . While the even spin excitations show a true gap which depends on doping, the odd spectrum is characterized by a weakly doping-dependent pseudogap. Both even and odd components are substantially enhanced upon lowering the temperature from 300 K. The even excitations evolve smoothly through the superconducting transition temperature  $T_c$ , but the odd excitations develop a true gap below  $T_c$ . At the same time, the odd spin susceptibility is sharply enhanced below  $T_c$  around an energy that increases with doping. This anomaly in the magnetic spectrum is closely related to the magnetic resonance peak that appears at 40 meV in the superconducting state of the optimally doped compound ( $T_c = 93$  K). From these data we extract the energy and the energy-integrated spectral weight of the resonance peak in absolute units as a function of doping level. Theoretical implications of these measurements are discussed, and a critique of recent attempts to relate the spin excitations to the thermodynamics of high temperature superconductors is given.

PACS numbers: 74.25.Ha, 74.60.w, 25.40.Fq, 74.72.Bk

## I. INTRODUCTION

The importance of electronic correlations in the copper oxide high temperature superconductors is now generally recognized. Some of the strongest evidence has been provided by neutron scattering measurements of the spin excitations in several families of cuprates:  $\text{La}_{2-x}\text{Sr}_x\text{CuO}_4$  [1],  $\text{YBa}_2\text{Cu}_3\text{O}_{6+x}$  [2–21], and recently also  $\text{Bi}_2\text{Sr}_2\text{CaCu}_2\text{O}_{8+\delta}$  [22]. While in an uncorrelated metal the spin excitation spectrum takes the form of a broad continuum extending up to energies comparable to the Fermi energy, the spin excitations in the metallic copper oxides in many ways resemble the antiferromagnetic magnons in their insulating parent compounds. This is illustrated by the mere fact that spin excitations cannot be observed at all in the metallic materials by neutron scattering: the spectral weight of continuum excitations in an uncorrelated metal is more than an order of magnitude below the sensitivity limit of current neutron instrumentation. In this article we continue our program of putting this qualitative observation on a quantitative footing by converting the neutron cross section to the absolute spin susceptibility.

The optimally doped superconductors  $\text{YBa}_2\text{Cu}_3\text{O}_7$  and  $\text{Bi}_2\text{Sr}_2\text{CaCu}_2\text{O}_{8+\delta}$  with transition temperatures in

the 90 K range at first sight appear compatible with a weak correlation picture as the normal-state spin susceptibility is indeed too weak to be measurable with the instrumentation currently available [10, 11, 18, 22]. However, below the superconducting transition temperature both compounds develop a remarkably sharp “resonance peak” at an energy of 40 meV whose spectral weight is comparable to that of antiferromagnetic magnons at the same energy [5–10]. This discovery, which was followed up by related observations in underdoped  $\text{YBa}_2\text{Cu}_3\text{O}_{6+x}$  [12–14] has generated much theoretical work, most of which is based on strong-correlation models [27–45]. Kinetic energy effects such as band structure singularities [29, 30, 46] or the manifestations of interlayer pair tunneling along the c-axis [47] have, however, also been implicated. The resonance peak has not been observed in conventional superconductors, but some recent data on heavy fermion compounds appear to have a similar signature [51]. Here we give a comprehensive account of this unusual phenomenon that provides important clues to the mechanism of high temperature superconductivity. We fully describe the evolution of its energy and spectral weight with hole concentration and elucidate the relationship of the resonance peak to the normal state excitations in the underdoped regime.

Our new experiments are generally consistent with pre-

vious investigations of the spin dynamics in the underdoped regime [2–5, 7, 8], but due to the combination of large single crystals and advanced neutron instrumentation the energy range could be extended above 100 meV, comparable to the nearest-neighbor antiferromagnetic superexchange energy  $J$  in the insulator, and the statistics could be substantially improved. Due to the extended energy range, we were able to probe not only the low energy sector of the spin excitation spectrum which evolves out of in-phase precession modes of spins in directly adjacent layers of the antiferromagnetic insulator  $\text{YBa}_2\text{Cu}_3\text{O}_6$  (acoustic magnons, Ref. [2,52]), but also the higher energy sector evolving out of antiphase (optical) magnons [53]. In the metallic state we prefer to characterize these excitations by their symmetry (odd or even, respectively) under exchange of the two layers. Observation of excitations in both sectors is important because it throws light on interlayer interactions within a bilayer both in the normal and in the superconducting states, an issue that has emerged as an important theme in the theory of high temperature superconductivity.

The article is organized as follows. In Section II we introduce our notation and the absolute scale which underlies much of the presentation. Technical details of the sample characterization and the neutron experiments are given in Sections III and IV, respectively. Section V gives a comprehensive account of the results on even and odd excitations in the normal state, and the spin gap and magnetic resonance peak in the superconducting state. The data are discussed in Section VI in the light of recent model calculations. Preliminary accounts of this work have been given in [13, 15–18].

## II. DEFINITIONS AND NOTATION

### A. Magnetic Susceptibilities and Absolute Units

Throughout this paper, wave vectors are expressed in reciprocal lattice units (r.l.u.), that is,  $\mathbf{Q} = H\mathbf{a}^* + K\mathbf{b}^* + L\mathbf{c}^*$  with  $\mathbf{a}^* \sim \mathbf{b}^* \sim 1.63\text{\AA}^{-1}$  and  $\mathbf{c}^* \sim 0.57\text{\AA}^{-1}$ . In these units, the antiferromagnetic zone center commonly referred to as  $\mathbf{Q}_0 = (\pi, \pi)$ , is at  $\mathbf{Q}_0 = (\frac{1}{2}, \frac{1}{2})$ . The two-dimensional reduced wave vector, modulo  $\mathbf{Q}_0$ , is denoted by  $\mathbf{q}$ .

Magnetic neutron scattering probes the imaginary part of the magnetic susceptibility tensor [54],

$$\frac{d^2\sigma}{d\Omega dE} = r_0^2 \frac{k_f}{k_i} f^2(\mathbf{Q}) \exp(-2W(\mathbf{Q})) \frac{N}{\pi(g\mu_B)^2} [1 + n(\omega)] \sum_{\alpha\beta} (\delta_{\alpha\beta} - \frac{Q_\alpha Q_\beta}{Q^2}) \chi''_{\alpha\beta}(\mathbf{Q}, \omega) \quad (1)$$

where  $r_0$  is the classical electron radius,  $\mathbf{k}_i$  and  $\mathbf{k}_f$  are the wave vectors of the incident and scattered neutron with  $\mathbf{Q} = \mathbf{k}_f - \mathbf{k}_i$ ,  $\alpha, \beta$  are the spatial components of the tensor,  $f(\mathbf{Q})$  is the atomic form factor of the orbitals that

contribute to the inelastic process,  $W(\mathbf{Q})$  is the Debye-Waller exponent, and  $N$  is the number of spins in the system. The susceptibility is related to the spin-spin correlation function in the form:

$$S_{\alpha\beta}(\mathbf{Q}, \omega) = \frac{1}{2\pi\hbar N} \sum_{ij} \int dt e^{i\mathbf{Q}\cdot(\mathbf{R}_j - \mathbf{R}_i) - i\omega t} \langle \hat{S}_i^\alpha \hat{S}_j^\beta(t) \rangle = \frac{1 + n(\omega)}{\pi(g\mu_B)^2} \chi''_{\alpha\beta}(\mathbf{Q}, \omega) \quad (2)$$

where  $S_i$  is the usual spin operator at site  $\mathbf{R}_i$ . It will often be fruitful to refer to this quantity because there is a sum rule for it (see Eq. 11 below).

When there is no magnetic long range order in the system and no preferred orientation, the summation in Eq. 1 must be rotationally invariant, that is,  $\sum_{\alpha\beta} (\delta_{\alpha\beta} - \frac{Q_\alpha Q_\beta}{Q^2}) \chi''_{\alpha\beta}(\mathbf{q}, \omega) = 2\text{Tr}(\chi''_{\alpha\beta})/3$ . Therefore, using the isotropic susceptibility  $\chi'' \equiv \text{Tr}(\chi''_{\alpha\beta})/3$ , Eq. 1 becomes for a magnetically disordered system

$$\frac{d^2\sigma}{d\Omega dE} = 2r_0^2 \frac{k_f}{k_i} f^2(\mathbf{Q}) \exp(-2W(\mathbf{Q})) \frac{1 + n(\omega)}{\pi(g\mu_B)^2} \chi'' \quad (3)$$

We had already used this definition previously [15]. However, in an earlier paper, some of us [11] used a slightly different convention for the dynamical susceptibility:

$$\frac{d^2\sigma}{d\Omega dE} = r_0^2 \frac{k_f}{k_i} f^2(\mathbf{Q}) \exp(-2W(\mathbf{Q})) (1 + n(\omega)) \frac{\hat{\chi}''}{3} \quad (4)$$

so that  $\chi'' = (2\pi\mu_B^2/3) \hat{\chi}''$ . The current convention agrees with the work of Hayden *et al.* [55] in the metallic state of  $\text{La}_{2-x}\text{Sr}_x\text{CuO}_4$  as well as with their recent work in  $\text{YBa}_2\text{Cu}_3\text{O}_{6+x}$  [56]. Throughout this paper,  $\chi''(\mathbf{Q}, \omega)$  is given in  $\mu_B^2/\text{eV}/[\text{unit formula}]$ .

The signal detected in a neutron scattering experiment is proportional to the intrinsic  $\chi''$  convoluted with the instrumental resolution function. We extract  $\chi''(\mathbf{Q}, \omega)$  from the data using a model of the resolution function and convert the result to absolute units through a calibration against selected phonons (see Appendix). Depending on the structure of the magnetic spectrum in momentum space, it is often convenient to further process the data by integrating  $\chi''$  over momentum or energy. We henceforth often use the spectral weight, here defined as  $\int d(\hbar\omega) \chi''(\mathbf{Q}_0, \omega)$ , as well as the Brillouin zone averaged susceptibility  $\chi''_{2D}(\omega)$ , also known as local susceptibility, defined as

$$\chi''_{2D}(\omega) \equiv \frac{\int d^2q \chi''(\mathbf{q}, \omega)}{\int d^2q} \quad (5)$$

The latter quantity is often used for systems with dispersing excitations. In particular, for a two-dimensional (2D) Heisenberg antiferromagnet, we have at low energies (where the magnon dispersion relation is approximately linear in wave vector):

$$\chi''_{2D}(\omega) \sim 4SZ_\chi \mu_B^2/J \sim 10 \mu_B^2/\text{eV}, \quad (6)$$

independent of energy. We here used the theoretical value of quantum corrections for  $S = \frac{1}{2}$ ,  $Z_\chi = 0.51$  [57], although neutron scattering experiments in several undoped cuprates [55, 58] indicate a systematic reduction of  $\sim 30\%$  of the spin-wave spectral weight as compared with the theoretical estimate (possibly due to covalency effects). Nevertheless, Eq. 6 provides a useful benchmark for the “oscillator strength” of normal state magnetic excitations in the metallic cuprates. The magnetic resonance peak in the superconducting state, on the other hand, is a non-dispersive excitation centered around a single point  $\mathbf{Q}_0$  in momentum space. As it is very narrow in energy, the instrumental resolution function carries out a partial energy-integration so that its spectral weight is best expressed in terms of  $\int d(\hbar\omega) \chi''(\mathbf{Q}_0, \omega)$ .

### B. Even and Odd Excitations

$\text{YBa}_2\text{Cu}_3\text{O}_{6+x}$  is a bilayer system, that is, two closely spaced copper oxide layers are separated by a much larger distance. Information about the magnetic coupling between the layers has been obtained from studies of the spin wave dispersions in insulating  $\text{YBa}_2\text{Cu}_3\text{O}_{6.2}$ . The superexchange coupling between adjacent bilayers is more than four orders of magnitude smaller than the primary energy scale,  $J \sim 100$  meV [2, 52]. In metallic  $\text{YBa}_2\text{Cu}_3\text{O}_{6+x}$ , where the in-plane correlation length is never larger than a few lattice spacings, the bilayers are therefore expected to be magnetically decoupled from each other, so that the neutron scattering signal is an incoherent superposition of the signals arising from individual bilayers. This is in accord with the experimental situation.

The intra-bilayer coupling  $J_\perp \sim 10$  meV [53], on the other hand, is only an order of magnitude below the intralayer superexchange, and it has long been known that even in the metallic regime the two layers within a bilayer remain strongly coupled [2–4, 7]. One focus of the present study is to further elucidate this magnetic inter-layer coupling.

To this end, we consider an eigenstate  $|n\rangle$  of the in-plane crystal momentum centered on the layer  $n$ . We can then define symmetric and antisymmetric combinations of states centered on the two layers within a bilayer:

$$\begin{aligned} |s\rangle &= (|1\rangle + |2\rangle)/\sqrt{2} \\ |a\rangle &= (|1\rangle - |2\rangle)/\sqrt{2} \end{aligned} \quad (7)$$

In this new basis, elementary excitations can be characterized by transitions between states of the same or opposite symmetry (even or odd excitations, respectively). The contribution of these two types of transition between spin states to the neutron scattering signal can be varied deliberately by adjusting the momentum transfer component  $Q_z$  perpendicular to the copper oxide layers. In particular, with layer states  $|1\rangle$  and  $|2\rangle$ ,

$$\begin{aligned} \hat{z}|1\rangle &= d/2|1\rangle \\ \hat{z}|2\rangle &= -d/2|2\rangle \\ \langle a, s | e^{iQ_z \hat{z}} | a, s \rangle &= \cos(Q_z d/2) \text{ (even)} \\ \langle s, a | e^{iQ_z \hat{z}} | a, s \rangle &= i \sin(Q_z d/2) \text{ (odd)} \end{aligned} \quad (8)$$

where  $d$  is the intrabilayer distance. Therefore, the intensities of the odd and even excitations, regardless of their in-plane wave vector and energy dependence, follow the  $\sin^2(Q_z d/2)$  and  $\cos^2(Q_z d/2)$  modulation, respectively, and we can write, following Eq. 2,

$$\begin{aligned} \chi''(\mathbf{Q}, \omega) &= \chi''_{\text{odd}}(\mathbf{q}, \omega) \sin^2(Q_z d/2) \\ &\quad + \chi''_{\text{even}}(\mathbf{q}, \omega) \cos^2(Q_z d/2). \end{aligned} \quad (9)$$

In the antiferromagnetic insulator,  $\chi''_{\text{odd}}$  and  $\chi''_{\text{even}}$  correspond to the acoustic and optical spin-waves, respectively [53]. The local and the energy-integrated susceptibilities as defined in the previous subsection can likewise be decomposed into their even and odd components.

### III. CRYSTAL SYNTHESIS AND CHARACTERIZATION

Our samples are three single crystals of volume  $\sim 1 - 3$  cm<sup>3</sup>. A precursor powder was made by combusting a stoichiometrically mixed aqueous solution of nitrates with sucrose. The powder was then calcined in a fully ventilated environment at 940°C for 6 hours to form YBCO powders. Crystals were grown using top seeded sintering techniques [23]. After fully oxygenating the resulting crystal by annealing in a pure oxygen environment, oxygen was systematically removed by progressive annealing under argon flow until the desired fraction of oxygen remained. They were then sealed in an evacuated quartz tube and annealed for two weeks to ensure homogeneity. We estimate the oxygen content by the weight gain/loss of the sample during the anneal, in conjunction with comparing to the  $T_c$  calibration of Cava *et al.* [59]. Several factors contribute to a rather large systematic error ( $\Delta x \sim \pm 0.05$ ) in the estimate of the absolute oxygen content. For instance, a significant fraction of a foreign phase ( $\text{Y}_2\text{BaCuO}_5$ , the so-called green-phase) embedded in the single crystal matrix makes it difficult to translate the weight change of the crystal into a change in stoichiometry. Three crystals were used:  $\text{YBa}_2\text{Cu}_3\text{O}_{6.5}$  with  $T_c \sim 52$  K and mass 23.3 g,  $\text{YBa}_2\text{Cu}_3\text{O}_{6.7}$  with  $T_c \sim 67$  K and mass 14.8 g, and  $\text{YBa}_2\text{Cu}_3\text{O}_{6.85}$  with  $T_c \sim 87$  K and mass 9.5 g.

The superconducting properties of these samples were characterized by SQUID magnetometry. The sharpness of the diamagnetic transition is usually a good indicator, but by no means a guarantee, of the uniformity of the oxygen distribution in a large crystal. A surface sheet of high oxygen content material with a high  $T_c$  may in principle mask more poorly superconducting material in the interior. At the expense of reducing the sample volume,

the SQUID measurements on the  $\text{YBa}_2\text{Cu}_3\text{O}_{6.5}$  sample were therefore performed on a piece cut from the interior of the sample. Details of these measurements have been given elsewhere [13]. On the  $\text{YBa}_2\text{Cu}_3\text{O}_{6.7}$  sample, we have, in addition, employed a nondestructive neutron depolarization technique that is sensitive to the distribution of superconducting transition temperatures throughout the bulk of the sample. This method is described in Section IV below.

#### IV. EXPERIMENTAL DETAILS

The crystals were aligned such that wave vector transfers of the form  $(H, H, L)$  or  $(3H, H, L)$  were accessible and loaded into a cryostat. The initial experiments were carried out at Brookhaven National Laboratory (BNL), on the H4M, H7 and H8 thermal triple axis spectrometers of the High Flux Beam Reactor. The bulk of the work was then carried out on the 2T spectrometer at the Laboratoire Léon Brillouin (LLB) for the  $\text{YBa}_2\text{Cu}_3\text{O}_{6.7}$  sample, and on the hot-neutron IN1 and thermal-neutron IN8 spectrometers at the Institut Laue-Langevin (ILL) for the  $\text{YBa}_2\text{Cu}_3\text{O}_{6.5}$  sample. Additional polarized-beam experiments were done on IN20 at the ILL. At BNL, we used pyrolytic graphite (PG) (002) monochromators and analysers with a PG filter in the scattered beam and neutrons of 30.5 meV fixed final energy. Collimations were set at 40-40-80-80. At the ILL, the incident beam was monochromated by a vertically focused Cu(111) crystal on IN8, and Cu(200) or Cu(220) with vertical focusing were used as monochromators on IN1. Vertically and horizontally focusing PG(002) was used as analyser. At LLB, we used a vertically curved Cu(111) monochromator and a vertically and horizontally focusing PG(002) analyser. Heusler(111) crystals were used in the polarization work at IN20. No beam collimations were used at the ILL and the LLB in order to maximize the benefits of focusing. A PG filter was placed behind the sample on 2T and IN8, and the final energy was fixed at 14.7, 30.5, or 35 meV depending on the range of excitation energies covered. An Erbium filter was used on IN1, and the final energy was fixed at 62.6 meV. The energy and momentum resolutions varied depending on the instrumental configuration used. Typical values for the energy resolution are 1 meV (full width at half maximum, FWHM) at energy transfer 5 meV, 5 meV at 50 meV, and 12 meV at 100 meV. The vertical resolution was typically  $0.35\text{\AA}^{-1}$  FWHM. Full four-dimensional resolution calculations were used to extract the intrinsic magnetic neutron cross section from the raw data.

The Heusler monochromator used in the polarized beam experiments [11,24] reflects only neutrons of a specific (vertical) spin polarization direction. Before impinging on the sample, the beam polarization is maintained (vertical field, VF) or rotated by  $90^\circ$  (horizontal field, HF) by homogeneous guide fields. After scat-

tering from the sample, the beam polarization is again maintained or rotated back by  $90^\circ$ , respectively. The beam then traverses a flipper (a set of coils capable of flipping the neutron spin polarization by  $180^\circ$ ), and the final beam polarization is analysed by a Heusler crystal which Bragg-reflects only neutrons whose polarization direction is the same as that of the original beam (after the monochromator). Because of limitations of the apparatus the beam polarization is always incomplete and is usually parametrized as  $(\text{FR}-1)/(\text{FR}+1)$ , where FR is the “flipping ratio”. When the flipper is on, the spin-flip (SF) cross section is measured, superposed by a polarization “leakage” contribution from non-spin-flip (NSF) scattering events (mostly phonon scattering), a contribution from nuclear spin incoherent scattering (NSI), and an extrinsic background (B). Because of polarization terms in the coherent magnetic scattering cross section [24] only half of the magnetic contribution (M) is measured for vertical guide field, whereas for HF the full contribution is measured. When the flipper is on and the flipping ratio is not too small, one obtains [24]

$$\begin{aligned} I_{\text{HF}} &= M + \frac{2}{3}\text{NSI} + \frac{\text{NSF}}{\text{FR}} + B \\ I_{\text{VF}} &= \frac{1}{2}M + \frac{2}{3}\text{NSI} + \frac{\text{NSF}}{\text{FR}} + B \end{aligned} \quad (10)$$

The standard method of extracting the magnetic contribution to the cross section is to subtract  $I_{\text{VF}}$  from  $I_{\text{HF}}$ , which yields  $M/2$ .

We used this setup on IN20 in order to determine the superconducting transition temperature of one of our large single crystals ( $\text{YBa}_2\text{Cu}_3\text{O}_{6.7}$ ) nondestructively and *in situ*. The technique relies on the fact that a spin-polarized neutron beam is depolarized when transiting a region containing a magnetic field whose direction varies on a short length scale, such that the neutron spins do not follow the change in field direction adiabatically. Depolarization is negligible only if the parameter  $\eta = \gamma B/v \frac{d\theta}{dx} \gg 1$ , where  $\gamma = 1.8 \times 10^8 \text{T}^{-1}\text{sec}^{-1}$  is the neutron gyromagnetic ratio,  $B \sim 10 \text{G}$  the applied field,  $v \sim 2000 \text{m/sec}$  the neutron velocity, and  $\frac{d\theta}{dx}$  the directional variation of  $B$  [25]. The spectrometer is set for a nuclear Bragg reflection. The field  $B$  is applied at the sample position in the same direction as the guide field before and after the sample, so that the beam polarization is maintained over the neutron flight path and the full nuclear Bragg intensity is detected. This remains unchanged as the sample is field-cooled through the superconducting transition. Because of the porous microstructure of our samples due to inclusions of a second phase,  $\text{Y}_2\text{BaCuO}_5$ , magnetic flux penetrates even at low fields and gets trapped by microstructural defects such as twin boundaries and the  $\text{Y}_2\text{BaCuO}_5$  inclusions. This flux has the same direction as the guide field and therefore does not depolarize the beam. The field is subsequently turned by  $90$  degrees at low temperature. Because of flux pinning, the vortices do not follow this change of field orientation, so that the net field at the sample position is

no longer parallel to the guide field. Significant beam depolarization results because  $\frac{d\theta}{dx} \sim \frac{\pi/2}{1\text{cm}}$ , where 1 cm is a typical sample dimension, and hence  $\eta < 1$ . The measured intensity of the nuclear Bragg reflection is therefore reduced (Fig. 1). Heating the sample in this state and monitoring the Bragg intensity provides a  $T_c$ -curve characteristic of the entire bulk of the sample. The small transition width shown in Fig. 1 attests to the high quality of the  $\text{YBa}_2\text{Cu}_3\text{O}_{6.7}$  sample.

While neutron scattering with polarization analysis is the most powerful tool to study magnetic excitations, current instrumentation restricts its use to rather low energy transfers (below  $\sim 50$  meV). Moreover, the neutron flux is substantially lower than in a standard unpolarized-beam experiment. For an extensive survey of the magnetic spectrum, and for higher excitation energies, inelastic neutron scattering experiments without polarization analysis are the only option. In unpolarized-beam experiments, the dynamic structure factor of phonons can exhibit various features in momentum space that can be mistaken for magnetic fluctuations at the worst, or complicate background subtraction at the very least. In order to arrive at a reasonable description of the phonon background, we numerically modeled the lattice dynamics of  $\text{YBa}_2\text{Cu}_3\text{O}_{6+x}$  using a simple harmonic interaction model. Once the phonon dispersion relations and eigenvectors are known as a function of wave vector, their full cross section can be calculated in absolute units. This has the added benefit of providing a standard against which the magnetic cross section can be calibrated. In previous publications, we have demonstrated the success of this model in predicting the cross section of a particularly important phonon at 42.5 meV [9, 11]. We have since augmented our calibration procedure by including several acoustic phonons, and we have further improved the parameters used in the simulation. Details are given in the Appendix.

We do not attempt to fit the whole phonon spectrum with our somewhat simplified model of the lattice dynamics which is still not completely understood [60]. Nevertheless, the simulation has given us a useful guide to extract the magnetic signal in some situations. As an example, Fig. 2 shows a “worst-case” scan at 55 meV, an energy range in which the phonon cross section is particularly large in the region of momentum space where the magnetic cross section is peaked. This excitation energy is too large for polarized-beam experiments. The figure shows that the model calculation allows us to extract the magnetic cross section from the data with some confidence even in this energy range. The dashed-dotted line describes the prediction of the phonon model which accounts well for the bowl-shaped background of the scan. The peak in the center of the scan, on the other hand, is not described by the phonon model and can therefore be recognized as magnetic.

Also, in many cases, additional elements such as the momentum dependence of the neutron intensity over

several Brillouin zones, its temperature dependence, its behavior upon changing the resolution conditions, etc., have been employed to cross-check the determination of the magnetic scattering. Such empirical methods have been discussed and successfully applied in previous studies [10, 14].

## V. RESULTS

Typical constant-energy scans (whose background is generally much more benign than that in Fig. 2) are shown for  $\text{YBa}_2\text{Cu}_3\text{O}_{6.5}$  in Fig. 3 and for  $\text{YBa}_2\text{Cu}_3\text{O}_{6.7}$  in Fig. 4. Several qualitative features are already apparent from the raw data. First, while the magnetic signal is always peaked at or near  $\mathbf{Q}_0 = (\pi, \pi)$ , the detailed shape of the profiles in momentum space depends on the excitation energy. As the excitation energy increases, the peak generally broadens, and at least in the  $\text{YBa}_2\text{Cu}_3\text{O}_{6.5}$  sample it begins to disperse away from  $\mathbf{Q}_0$  above 50 meV (Fig. 3). The line shape will be discussed in Section V C below. Second, the even spin excitations (shown in Fig. 4) are fully gapped, as are the even excitations (optical spin waves) in the antiferromagnetic insulator. The data were fitted to single or double Gaussians, as appropriate, and corrections for the resolution function were made.

The data were further corrected for the magnetic form factor of copper. Because of the energy dependence of the momentum line shape ( Figs. 3-4), we plot in Figs. 5 and 6 the  $\mathbf{q}$ -averaged (local) susceptibility ( $\chi''_{2D}$ , Eq. 5) of the two samples in the even and odd channels, derived from the fitted intensities and widths of the Gaussian profiles. Alternatively, the data can be summarized in terms of the peak intensity at  $\mathbf{Q}_0$ , as shown for  $\text{YBa}_2\text{Cu}_3\text{O}_{6.7}$  in Fig. 7. The local and peak susceptibilities are not proportional to each other, because of the energy dependence of the momentum line shape. Note also that the absolute magnitudes of the susceptibilities in Figs. 6 and 7 differ by more than order of magnitude, because the susceptibility is always strongly peaked at or near  $\mathbf{Q}_0$ . Nevertheless, the qualitative features of Figs. 5 and 7 are similar. The spin excitations in the  $\text{YBa}_2\text{Cu}_3\text{O}_{6.85}$  crystal are restricted to a much smaller energy range than in  $\text{YBa}_2\text{Cu}_3\text{O}_{6.5}$  and  $\text{YBa}_2\text{Cu}_3\text{O}_{6.7}$ , as observed previously [3]. A full spectrum is reported in a forthcoming publication [26].

### A. Magnetic Resonance Peak and Superconducting Energy Gap

One of the most striking features of the data of Figs. 5a-7a is a pronounced peak that develops at low temperatures. Various features of this peak are strongly reminiscent of the magnetic resonance peak that was observed at an excitation energy of 40 meV in optimally

doped  $\text{YBa}_2\text{Cu}_3\text{O}_{6+x}$  [5–10] and more recently also in  $\text{Bi}_2\text{Ca}_2\text{CuSr}_2\text{O}_{8+\delta}$  [22]: it is concentrated around a single point in an energy-wave vector diagram, its intensity decreases with increasing temperature, and it occurs in the odd channel. This analogy is further bolstered by considering the detailed temperature dependence of the peak local susceptibility that is shown in Fig. 8 for both samples. Clearly, the intensity is sharply enhanced below a temperature that, to within the experimental error, is identical to  $T_c$  in both cases. The coupling to superconductivity is another characteristic feature of the resonance peak in the optimally doped compounds. We can therefore clearly associate the enhancement of the dynamical susceptibility in the underdoped samples below  $T_c$  with the magnetic resonance peak.

As was noted earlier [12–14], the energy of the resonance peak decreases systematically as the hole concentration is lowered from optimal doping. Another difference between the optimally doped and underdoped materials is that in the latter samples magnetic excitations are detectable in the normal state. The buildup of the magnetic correlations, though strongly enhanced in the superconducting state in a narrower energy window, already begins much above  $T_c$ . Indeed, the response shown in Figs. 5–7 is already broadly peaked in the normal state. The normal state spectra are discussed in detail in Section VB below.

For now, we focus on the enhancement of the dynamical susceptibility below  $T_c$ . In order to elucidate the influence of superconductivity on the magnetic excitation spectra, we have subtracted the data just above their respective  $T_c$  from the data deep in the superconducting state. The result is shown in Figs. 9 and 10 in the form of  $\chi''(\mathbf{Q}_0, \omega)$  as well as  $S(\mathbf{Q}_0, \omega)$ . In this context it is fruitful to consider the latter quantity because it is constrained by a sum rule:

$$\frac{\int d^3Q d(\hbar\omega) \text{Tr}(S_{\alpha\beta}(\mathbf{Q}, \hbar\omega))}{\int d^3Q} = S(S+1) \text{ per Cu atom} \quad (11)$$

This so-called “total moment sum rule” is strictly valid only for the undoped Heisenberg antiferromagnet (with spin  $S = \frac{1}{2}$ ), and the numerical constant is likely to be somewhat reduced as holes are added in the metallic regime of the phase diagram. Independent of doping, however, the total moment sum rule implies that  $S(\mathbf{Q}, \omega)$ , integrated over all momenta and energies, is temperature independent. Note, however, that in a metallic system the relevant energies extend up to energies comparable to the Fermi energy, far beyond the energy range probed by our experiment.

Fig. 9b shows that for the  $\text{YBa}_2\text{Cu}_3\text{O}_{6.5}$  sample the enhancement of the spectral weight around 25 meV, which we attribute to the magnetic resonance peak, is accompanied by a reduction of spectral weight over a limited energy range both above and below 25 meV. The width of the response in momentum space does not

change significantly upon entering the superconducting state, and the reduction of spectral weight above and below the resonance peak compensates the resonant enhancement such that the total moment sum rule is satisfied to within the experimental error.

The  $\text{YBa}_2\text{Cu}_3\text{O}_{6.7}$  sample shows a qualitatively similar behavior, but within the energy range probed by our experiment the enhancement of the spectral weight around the resonance energy of  $\sim 33$  meV outweighs the reduction of spectral weight at other energies. This trend continues as the hole concentration is increased. In  $\text{YBa}_2\text{Cu}_3\text{O}_7$ , where normal state excitations have not been clearly identified, a loss of spectral weight accompanying the resonance peak has thus far not been observed. At least for doping levels exceeding  $x \sim 0.7$ , we therefore have to postulate a broad and weak continuum of excitations, perhaps extending up to high energies and not directly observed in our experiments, as a “reservoir” of quantum states from which the resonance peak is drawn.

Following these considerations, we have chosen to parameterize the spectral weight of the resonance peak by the positive component of the difference spectra of Figs. 9 and 10,  $\int d(\hbar\omega) \Delta\chi''_+(\mathbf{Q}_0, \omega)$ , in order to compare different doping levels. (Note that in the energy range in which the enhancement occurs, and over the temperature range considered, the Bose population factor  $1 + n(\omega)$  in Eq. 2 is very close to 1, so that  $\Delta\chi''_+$  and  $\Delta S_+$  are simply proportional to each other.) Fig. 11 summarizes the doping dependences of the spectral weight and energy of the resonance peak as a function of doping concentration. The large error bars attached to  $\Delta\chi''_+$  in Fig. 11 are in part due to ambiguities arising from the incommensurate response below the resonance peak which is discussed below. While the energy of the resonance peak increases with increasing doping level, the absolute spectral weight is more weakly doping dependent (though a clear reduction is observed in the fully oxygenated sample  $\text{YBa}_2\text{Cu}_3\text{O}_7$ ). Note also that the dynamical susceptibility in the normal state decreases strongly with increasing doping level. A feature not shown in Fig. 11 is the width of the magnetic resonance peak in energy which is comparable to the experimental energy resolution for  $\text{YBa}_2\text{Cu}_3\text{O}_{6.7}$ ,  $\text{YBa}_2\text{Cu}_3\text{O}_{6.85}$  and  $\text{YBa}_2\text{Cu}_3\text{O}_7$ , but broadened to an intrinsic width of  $\sim 10$  meV for  $\text{YBa}_2\text{Cu}_3\text{O}_{6.5}$ . It was shown in [21] that a small amount of disorder can lead to a drastic broadening of the peak, and we cannot exclude disorder in the Cu-O chain layer as the origin of the broadening in  $\text{YBCO}_{6.5}$ .

Although the  $\mathbf{q}$ -width of the resonance peak,  $\Delta\mathbf{q} = 0.25\text{\AA}^{-1}$ , does not depend significantly on doping, it is nonetheless interesting to compute the energy and wave vector integrated spectral weight of the resonance peak, and to compare the result to the total moment sum rule, Eq. 11. After a two-dimensional Gaussian integration of the difference signal, we obtain  $0.069\mu_B^2$ ,  $0.056\mu_B^2$ ,  $0.07\mu_B^2$ , and  $0.043\mu_B^2$  for  $\text{YBa}_2\text{Cu}_3\text{O}_{6.5}$ ,  $\text{YBa}_2\text{Cu}_3\text{O}_{6.7}$ ,  $\text{YBa}_2\text{Cu}_3\text{O}_{6.85}$ , and  $\text{YBa}_2\text{Cu}_3\text{O}_7$ , respectively. This

means that roughly 1-2% of the total magnetic spectral weight is redistributed to the magnetic resonance peak upon cooling below  $T_c$ .

Another important phenomenon at least partly associated with the superconducting state is the formation of a spin gap in the susceptibility spectrum with decreasing temperature. In the  $\text{La}_{2-x}\text{Sr}_x\text{CuO}_4$  superconductor, the normal state response is incommensurate and a small spin gap ( $\sim 3\text{-}6$  meV) is observed in the superconducting state [63,64]. In this system, the size of the spin gap seems to be a good indicator of the homogeneity of the samples; impurities apparently introduce new states below the spin gap, thereby smearing out the superconductivity-induced anomalies in both temperature and energy. This has also been confirmed experimentally in Zn-substituted  $\text{YBa}_2\text{Cu}_3\text{O}_{6+x}$  [65,66].

We have established the size of the spin gap in the superconducting state of  $\text{YBa}_2\text{Cu}_3\text{O}_{6.7}$  in a polarized-beam experiment. Polarization analysis is required for an accurate determination of the onset of magnetic scattering, as optical phonon scattering is rather strong in the vicinity of the spin gap. Fig. 12 shows typical constant-energy scans taken with a polarized beam, and Fig. 13 shows the low energy spectrum of  $\text{YBa}_2\text{Cu}_3\text{O}_{6.7}$  derived by fitting the constant-energy scans to Gaussians and plotting the amplitude versus energy. The large spin gap of  $\sim 17$  meV is testimonial to the quality of the samples. Its size agrees well with the measurements of Rossat-Mignod *et al.* on a  $\text{YBa}_2\text{Cu}_3\text{O}_{6.69}$  sample [2]. Similar measurements for  $\text{YBa}_2\text{Cu}_3\text{O}_{6.5}$  yield an energy gap of about 5 meV at low temperatures. The doping dependence of the superconducting spin gap is therefore quite different from that of the magnetic resonance peak itself, as already found previously [2-4].

## B. Normal State Susceptibility

Having established the influence of superconductivity on the spin excitations, we now describe their development with temperature and doping in the normal state. The general trends can be seen in Figs. 5 and 6, where the susceptibility is given in absolute units up to excitation energies of 120 meV. The low-energy spectra in the odd channel, which are consistent with previous work [2-4,7], show a broad peak whose amplitude decreases gradually with increasing temperature and doping. Figs. 5-7 demonstrate that the low energy spectral weight is already rather small in the normal state, and that the additional depression upon entering the superconducting state is rather subtle. (This was established for our samples in detailed studies of the temperature dependence of the low energies, not shown here.) This is consistent with prior neutron observations of the spin pseudo-gap in underdoped  $\text{YBa}_2\text{Cu}_3\text{O}_{6+x}$  [2] as well as in nuclear magnetic resonance (NMR) measurements [67,68]. The relationship between the magnetic resonance peak and

this normal state peak will be described in the next section. We here stress that one has to be cautious in interpreting the broad normal-state peak in the odd channel simply as a precursor of the magnetic resonance peak in the superconducting state.

Until recently, neutron studies of  $\text{YBa}_2\text{Cu}_3\text{O}_{6+x}$  have been confined to the odd channel, where excitations can be observed at relatively low energies. This situation was changed when Reznik *et al.* [53] identified even excitations (optical magnons) in the antiferromagnetic insulator. Although the coupling between two directly adjacent layers, extracted from an analysis of the spin wave dispersions, is only  $J_\perp \sim 10$  meV, antiferromagnetic long range order, together with the much larger intralayer exchange coupling of  $J \sim 100$  meV, boosts the gap for optical magnons to  $\sim 67$  meV. It is therefore interesting to monitor the odd-even splitting in the absence of long range order. Figs. 5b and 6b show that the even spectrum remains fully gapped even in the metallic regime, although the gap decreases and broadens with increasing doping.

Similar to the odd channel, the even excitations also exhibit a broad peak, albeit centered around a higher energy. The temperature evolution of the intensity around the peak position is given in Fig. 14 for  $\text{YBa}_2\text{Cu}_3\text{O}_{6.7}$  and compared to the intensity in the odd channel at the same energy. The even intensity increases markedly with decreasing temperature, whereas the odd intensity at this energy remains constant to within the error. The marked difference in even and odd response functions in this energy range is already quite apparent in the data of Fig. 4. The gradual increase is reminiscent of the gradual growth of the peak intensity in the odd channel in the normal state (Fig. 8), but no anomaly is observed in the even channel at  $T_c$ .

We summarize the temperature evolution of even and odd spectra schematically in Fig. 15. At high temperatures the dynamical susceptibility is rather featureless. Lowering the temperature leads to a gradual enhancement of the spin susceptibility in both even and odd channels at approximately the same rate, but centered around different frequencies. Just above  $T_c$ , both spectra therefore look very similar, with a broad peak in each channel that is merely shifted in frequency. Below  $T_c$ , the parallel evolution of both spectra ceases. The peak in the odd channel sharpens abruptly while the intensity in the even channel continues its smooth normal-state evolution and eventually saturates.

Finally, we draw attention to a noticeable dip in the odd channel excitation spectrum around 55 meV (Figs. 5 and 6) which we are unable to account for in our phonon simulation. Above this minimum the local susceptibility rises to a second (less pronounced) maximum. This behavior is in qualitative agreement with pulsed neutron data in  $\text{YBa}_2\text{Cu}_3\text{O}_{6.6}$  [56]. (Note, however, that the intensity above 70 meV reported in Ref. [56] is twice as large as ours even though both data sets agree in the low energy range). The dip is observed in both underdoped

samples but is more pronounced in  $\text{YBa}_2\text{Cu}_3\text{O}_{6.5}$ . It is tempting to associate this feature with the gap in the even spectrum that also occurs in this energy range. A more detailed analysis of the spectra reveals, however, that the gap in the even channel has a stronger doping dependence than the 55 meV feature in the odd channel, which makes this scenario unlikely. We briefly discuss alternative explanations in Section VI below. Unfortunately, the dip feature occurs in an energy region with a nontrivial phonon background (Fig. 2) and at an energy too high for polarization analysis. A detailed experimental characterization is therefore difficult.

### C. Momentum Line Shape

In the context of recent debates about the role of “charge stripe” fluctuations in high temperature superconductivity, the momentum line shape of the spin response in  $\text{YBa}_2\text{Cu}_3\text{O}_{6+x}$  has emerged as an important issue. Early indications of an incommensurate response [8] were followed up by more detailed investigations over a narrow range of energies and doping levels [19, 20]. Because of the coarse vertical resolution of a triple axis spectrometer and the nontrivial phonon background, special precautions are required to clearly resolve the incommensurate response in  $\text{YBa}_2\text{Cu}_3\text{O}_{6+x}$ . This is not the primary focus of the present study; ongoing detailed measurements of this aspect are focused on the  $\text{YBa}_2\text{Cu}_3\text{O}_{6.85}$  sample, where the incommensurate response is most pronounced, and will be reported separately in a forthcoming publication [26]. Here we discuss some generic features of the momentum line shape that are apparent without high momentum resolution.

Independent of the detailed line shape, an important parameter for the purposes of the present study is the overall extent in momentum space of the magnetic response at a given energy. For instance, this quantity enters into our determination of the local susceptibility of Figs. 5 and 6. This overall width was extracted from the constant-energy profiles by fitting them to either a single Gaussian centered at  $\mathbf{Q}_0 = (\pi, \pi)$ , or if necessary, to two Gaussians symmetrically displaced around  $\mathbf{Q}_0$ . Fig. 16 gives the result of this procedure for our  $\text{YBa}_2\text{Cu}_3\text{O}_{6.7}$  sample. While most profiles are adequately fit by a broad single peak, we paid particular attention to the energy range around 24 meV, just below the resonance peak, and were able to confirm the recent observation [19] of an incommensurate response. The weakly energy dependent  $\mathbf{q}$ -width below the resonance peak has been noticed before [2, 7, 14, 62] and may reflect an incommensurate response which is unresolved due to the coarse resolution. At the resonance energy, the overall  $\mathbf{q}$ -width goes through a minimum which is particularly noticeable when considering the resonant response only (that is, the  $\mathbf{q}$ -width of the additional intensity peak below  $T_c$ , Fig. 10) [10].

The pronounced intrinsic broadening at high energies

above 50 meV cannot be attributed to resolution effects and is reminiscent of the dispersion-like behavior observed in  $\text{YBa}_2\text{Cu}_3\text{O}_{6.5}$  (Fig. 3, see also [15]) which in turn resembles the dispersion of antiferromagnetic magnons. It is interesting to notice that the onset of this broadening coincides with the peak-dip feature in Figs. 5 and 6. In this high energy region, the primary effect of hole doping therefore appears to be a strong broadening of the magnetic response. Overall, Fig. 16 is in good agreement with the recent report by Arai *et al.* [61] on a sample with a similar  $T_c$ . (Note, however, that these authors chose to fit all of their constant-energy profiles to double peaks.)

## VI. DISCUSSION

The most striking feature in the neutron spectra of  $\text{YBa}_2\text{Cu}_3\text{O}_{6+x}$  is the magnetic resonance peak whose experimental properties are summarized in Fig. 11. This phenomenon has been addressed in numerous theoretical studies over the past few years. One purpose of the present article is to present a summary of the current state of experimental information on the resonance peak. The other purpose is to stimulate further theoretical work on the interplay between normal state excitations and the resonance peak in the underdoped regime. We discuss these two aspects in turn.

Compared to the broad continuum expected for ordinary metals, the resonance peak involves an extraordinarily small volume of phase space.  $d$ -wave superconductivity helps explain this observation: The coherence factor in the neutron scattering cross section has a pronounced maximum at a wave vector connecting two lobes of the  $d$ -wave gap function with opposite sign of the order parameter [9]. (An early interpretation based on a different gap symmetry [27] has been ruled out by a variety of other measurements [69].) It has since turned out that  $d$ -wave superconductivity alone is not sufficient to explain the sharpness and spectral weight of the resonance peak, and that other factors further narrow the phase space involved in this process. Strong Coulomb interactions between electrons are the most likely factor.

Some of the features of the resonance peak can be described in models that do not include such interactions. For instance, early photoemission studies have suggested an extended saddle point singularity near the Fermi level [70]. It has been shown that this band structure anomaly leads to a peak in the joint density of states, which in turn produces a peak in the unrenormalized susceptibility  $\chi_0''$  [30, 46]. The peak grows as the gap opens in the superconducting state. The peculiar gap structure in the interlayer tunneling model of high temperature superconductivity also leads to a rather sharp peak in  $\chi_0''$  in the superconducting state [47]. The peak position is determined by a combination of the energy gap and the chemical potential (see, e.g., Ref. [33]) so that



even in this minimalist model the resonance peak and the superconducting energy gap do not have to show the same doping dependence [36]. The resonance peak energy *decreases* as the hole concentration is lowered from the optimally doped state (Fig. 11) while the energy gap, which is directly determined by photoemission and other techniques, remains constant or increases (see, e.g., [71]). However, the interplay between the pseudo-gap measured in the normal state and the superconducting gap is not well understood at present in these experiments.

There are, however, strong indications that electron correlations are necessary for an adequate description of the resonance peak. First, the absolute magnitude of the dynamical susceptibility, determined experimentally in Refs. [11,15], is too large to be consistent with the relatively subtle enhancement assumed in Refs. [46,47]. This does not necessarily rule out the mechanisms proposed in this work, but it strongly suggests that Coulomb correlations are also needed to reproduce the experimentally measured  $\chi''$ . Second, the sharpness of the resonance peak close to optimal doping indicates a true collective mode. This is indeed the direction that most of the recent theoretical work has taken.

The theoretical description of this collective mode remains a subject of considerable controversy. In one theoretical approach, the peak is identified with a resonance in the particle-particle channel. Proponents of this model [40], later embedded into a more comprehensive theory of high temperature superconductivity [41,42], early on predicted the resonance spectral weight to within a factor of two of the measured number for optimally doped  $\text{YBa}_2\text{Cu}_3\text{O}_{6+x}$  [11]. In the framework of this theory, the resonance can be viewed as a pseudo-Goldstone boson of a new symmetry group encompassing antiferromagnetism and  $d$ -wave superconductivity. The symmetry becomes exact at the quantum critical point separating both phases, and the energy of the Goldstone boson approaches zero in accord with the data. This scenario is also consistent with the tendency of the resonance spectral weight to increase with decreasing hole concentration (Fig. 11). All of these features are, however, also consistent with a more conventional description in which the resonance occurs in the particle-hole channel. In this approach, the resonance is identified with a spin excitation that is stabilized when decay channels are removed in the superconducting state. Recent theoretical studies have shown that the evolution of the resonance energy and spectral weight with doping (Fig. 11) as well as the broadening of the resonance in the deeply underdoped regime can be explained in this framework [36,45]. It has also emerged that a remarkably consistent picture of ARPES and neutron data can be obtained in this framework [36,78,79]. An interesting suggestion put forth in this context is to interpret the weakly doping dependent dip-peak feature of Figs. 5 and 6 as a signature of the bare superconducting energy gap, while the resonance peak is pulled below the gap by interactions [79]. Further work is necessary to establish whether the onset of the

momentum-space broadening in this energy range (Section VC) can also be explained in this model. Finally, it has been proposed that the resonance peak originates from localized electrons in domain walls between charge stripes, separate from those that form the superconducting condensate [48]. While the large spectral weight of the peak finds a natural explanation in this approach, it is much harder to account for its sharpness in both energy and momentum and its strong coupling to superconductivity. Further, the evidence of charge stripes is weak in optimally doped  $\text{YBa}_2\text{Cu}_3\text{O}_7$  where the resonance peak is most pronounced.

We do not wish to reiterate the purely theoretical arguments that were advanced in this debate (see, e.g., [36,42,45,49,50]). Rather, we point to the additional experimental information presented in this article, much of which still awaits a theoretical explanation. We first discuss the normal state susceptibility described in Section VB and summarized schematically in Fig. 15. The broad peak in the odd channel that grows with decreasing temperature (already been observed in early work on underdoped  $\text{YBa}_2\text{Cu}_3\text{O}_{6+x}$  [2–4,7]) signifies a new energy scale in the normal-state spin excitation spectrum, different from the superexchange interaction  $J$  that sets the energy scale in the insulator. It was pointed out [37,75] that damping of antiferromagnetic spin waves (seen as long-lived excitations in the insulator) introduces such a new energy scale, namely  $\sim Ja/\xi$  (where  $\xi \sim 2a - 5a$ , depending on doping, is the spin-spin correlation length), above which the excitations are not substantially different from those of the insulator. This approach can describe some aspects of the data, especially the dispersion-like behavior observed at high energies in  $\text{YBa}_2\text{Cu}_3\text{O}_{6.5}$ . The response in the even channel is also qualitatively consistent with a description based on damped spin waves. When  $\xi$  is short, one may expect the even and odd response functions to be shifted by  $J_\perp \xi/a$ , the energy cost for flipping a correlated patch of spins in a single layer while keeping the spins in the neighboring layer fixed. (This simple estimate was confirmed by numerical simulations on finite-sized systems.) The actual situation (Figs. 5 and 6) interpolates between this limit and the antiferromagnetic long range ordered state with an optical magnon gap of  $2\sqrt{JJ_\perp} \sim 67$  meV [53].

The temperature dependence of the broad normal-state peak in the pseudo-gap regime and its relation to the magnetic resonance peak are more difficult to describe. Of course, short range dynamic spin correlations centered around  $\mathbf{Q}_0 = (\pi, \pi)$  are expected in a variety of microscopic strong-correlation models. The challenge is now to use these models to make detailed predictions of the temperature evolution of the magnetic spectra in both the superconducting and the normal states. Phenomenologically, the low-energy “overdamped spin wave” response grows with decreasing temperature. The broad peaks in both even and odd channels grow gradually and approximately at the same rate, while at the same time a spin pseudo-gap opens in the odd channel as already

revealed by earlier neutron [2, 7] and NMR [67] experiments. Although it is hard to associate a characteristic temperature with this crossover phenomenon, our data are certainly consistent with models that predict a correlated spin liquid phase below a doping dependent “coherence temperature”, often termed  $T^*$  [76].

It is important to draw a distinction between the gradual growth of the broad normal state peaks in both even and odd channels on the one hand, and the abrupt increase of the intensity in the superconducting state that occurs in the odd channel *only* on the other hand. This is seen most clearly in the high-statistics data of Fig. 8a. Though both are clearly related, a recent re-interpretation of the previously observed broad normal-state peak in the odd channel as a “pre-transitional precursor” of the resonance peak is therefore too simple-minded [56]. There is, moreover, no basis for a separation of resonant and non-resonant response functions in the normal state as proposed in Ref. [56]. Promising steps in the direction of a microscopic description of the spin dynamics in both normal and superconducting states have recently been taken (see, e.g., Ref. [43]).

This also bears directly on the issue of the origin of the superconducting condensation energy that has recently moved into the foreground of the high- $T_c$  debate. Scalapino and White [72] derived a formula that relates the exchange energy (associated with the  $J$ -term in the  $t - J$  model) to the magnetic excitation spectrum. If the complete spectrum is known in absolute units, the change in exchange energy between normal and superconducting states can be evaluated and quantitatively compared to the superconducting condensation energy determined in specific heat experiments [77]. In optimally doped  $\text{YBa}_2\text{Cu}_3\text{O}_{6+x}$ , the resonance peak is the only experimentally discernible feature in the magnetic spectrum, and its spectral weight is known in absolute units [11]. Since the normal state spectrum is unknown except for an upper bound guaranteeing that the amplitude of the normal state excitations is significantly below the resonance amplitude [10, 11, 18], it is reasonable to apply the Scalapino-White formula to the resonance peak only. This is the approach adopted by Demler and Zhang [73] who found that the magnetic energy stored in the resonance peak equals the superconducting condensation energy to within an order of magnitude. Temperature dependent changes in other parts of the spectrum, though not visible in the neutron experiments, could of course lead to quantitative modifications in this analysis. The full implications of this analysis for the pairing mechanism of high temperature superconductivity are, however, still under debate. Others [74] have argued, for example, that the neutron peak provides a measure of the condensate fraction, rather than the condensation energy, of the superconducting state.

The experimental situation is much less straightforward in the underdoped regime. We have shown here that the amplitude of the magnetic response in the normal state is at least as large as the resonance amplitude,

and that it is spread over a much larger energy range. If one wants to extend the Demler/Zhang analysis into the normal state of underdoped  $\text{YBa}_2\text{Cu}_3\text{O}_{6+x}$ , it is therefore erroneous to focus exclusively on the energy at which the resonance eventually develops in the superconducting state [56], especially since a separation of the normal-state response into resonant and nonresonant contributions is entirely arbitrary. It is also inappropriate to neglect the optical channel in such an analysis, because its amplitude and temperature dependence in the normal state are at least equal to those in the superconducting state. Because the Scalapino-White formula differs from the total moment sum rule (Eq. 11) only through a momentum-dependent form factor, any gain in magnetic energy must result from temperature dependent changes of the momentum line shape which are not even considered in Ref. [56]. It is easy to see that the outcome of an adequate analysis of the magnetic energy stored in the normal state spin excitations and its relation to the specific heat would likely be qualitatively different from the one given in Ref. [56]. In particular, the normal-state electronic specific heat in the pseudogap regime of the  $\text{YBa}_2\text{Cu}_3\text{O}_{6+x}$  phase diagram is actually *lower* than at optimum doping [77], whereas the magnetic spectral weight and its temperature dependence are clearly *larger* in underdoped samples. Because of insufficiently accurate information on the temperature dependence of the momentum line shapes, we have not used our spectra to attempt such an analysis ourselves.

In summary, we have presented a comprehensive account of the magnetic resonance peak and the normal state spin excitations in underdoped  $\text{YBa}_2\text{Cu}_3\text{O}_{6+x}$ . We hope that the detailed description of the magnetic spectra presented here will provide an improved basis for models of electronic correlations in the cuprates.

## ACKNOWLEDGMENTS

We wish to thank M. Braden at LLB and J. Kulda at ILL for their help during the experiments, and P.W. Anderson, A. Chubukov, V.J. Emery, B. Hennion, M. Norman, F. Onufrieva, and P. Pfeuty for stimulating discussions.

## APPENDIX A: PHONON SIMULATION

Empirical descriptions of the eigenvibrations in a single crystal are instrumental in obtaining the absolute magnitude of the dynamical susceptibility in our measurements. However, as there are 39 phonon branches in  $\text{YBa}_2\text{Cu}_3\text{O}_7$  spread over an energy range of roughly 70 meV, individual phonon branches are usually difficult to resolve (with a typical energy resolution of 5 meV). Fortunately, in past successful experiments, we have isolated one particularly strong phonon branch at

42.5 meV [9, 11]. Since then we have further reinforced confidence in our model by identifying and simulating acoustic phonon branches. Acoustic phonons are attractive for absolute unit measurements because their intensities are strongly related to the Bragg peak intensities. Unlike optical phonons, the most important quantity for the acoustic phonons is just one number—the limiting value of the structure factor as it approaches the Bragg condition. The convolution of their “cone shape” dispersion curve with the instrumental resolution has been performed analytically as well as by using an efficient sampling technique based on the fast Fourier transform to perform a four dimensional numerical convolution [80]. We have extensively used a longitudinal acoustic phonon branch around the (006) Bragg condition. Our simulation gives a structure factor of  $4.3 \times 10^{-18} c^2 \text{ eV}^{-1}$  which is consistent with our earlier optical phonon calibration measurements. We further point out that the calibration using phonon scattering from the sample avoids the difficulties related to existence of “green phase” impurities as well as inclusions of smaller crystallites inevitable in these large  $\text{YBa}_2\text{Cu}_3\text{O}_{6+x}$  samples. This may contribute to systematic errors when calibrating against a vanadium standard [55, 56].

- 
- [1] M.A. Kastner, R.J. Birgeneau, G. Shirane, and Y. Endoh, *Rev. Mod. Phys.* **70**, 897 (1998).
- [2] J. Rossat-Mignod, L.P. Regnault, P. Bourges, P. Burlet, C. Vettier, and J.Y. Henry, in *Selected Topics in Superconductivity*, edited by L.C. Gupta and M.S. Multani, *Frontiers in Solid State Science* (World Scientific, Singapore, 1993), p.265.
- [3] P. Bourges, in *The gap Symmetry and Fluctuations in High Temperature Superconductors* Edited by J. Bok, G. Deutscher, D. Pavuna and S.A. Wolf. (Plenum Press, 1998) 349 (cond-mat/9901333).
- [4] L.P. Regnault, P. Bourges and P. Burlet in *Neutron Scattering in Layered Copper-Oxide Superconductors*, Edited by A. Furrer, 85 (Kluwer, Amsterdam, 1998).
- [5] J. Rossat-Mignod, L.P. Regnault, C. Vettier, P. Bourges, P. Burlet, J. Bossy, J.Y. Henry, and G. Lapertot, *Physica C* **185-189**, 86 (1991).
- [6] H.A. Mook, M. Yethiraj, G. Aeppli, T.E. Mason, and T. Armstrong, *Phys. Rev. Lett.* **70**, 3490 (1993).
- [7] J.M. Tranquada, P.M. Gehring, G. Shirane, S. Shamoto, and M. Sato, *Phys. Rev. B* **46**, 5561 (1992).
- [8] B. J. Sternlieb, J. M. Tranquada, G. Shirane, M. Sato and S. Shamoto, *Phys. Rev. B* **50**, 12915 (1994).
- [9] H.F. Fong, B. Keimer, P.W. Anderson, D. Reznik, F. Dogan, and I.A. Aksay, *Phys. Rev. Lett.* **75**, 316 (1995).
- [10] P. Bourges, L.P. Regnault, Y. Sidis and C. Vettier, *Phys. Rev. B* **53**, 876 (1996).
- [11] H.F. Fong, B. Keimer, D. Reznik, D.M. Milius, and I.A. Aksay, *Phys. Rev. B* **54**, 6708 (1996).
- [12] P. Dai, M. Yethiraj, H.A. Mook, T.B. Lindemer, and F. Dogan, *Phys. Rev. Lett.* **77**, 5425 (1996).
- [13] H.F. Fong, B. Keimer, F. Dogan, and I.A. Aksay, *Phys. Rev. Lett.* **78**, 713 (1997).
- [14] P. Bourges, L.P. Regnault, Y. Sidis, J. Bossy, P. Burlet, C. Vettier, J.Y. Henry and M. Couach, *Europhys. Lett.* **38**, 313 (1997).
- [15] P. Bourges, H.F. Fong, L.P. Regnault, J. Bossy, C. Vettier, D.L. Milius, I.A. Aksay and B. Keimer, *Phys. Rev. B* **56**, R11439 (1997).
- [16] B. Keimer, H.F. Fong, S.H. Lee, D.L. Milius, I.A. Aksay, *Physica C* **282-287**, 232 (1997).
- [17] B. Keimer, I.A. Aksay, J. Bossy, P. Bourges, H.F. Fong, D.L. Milius, L.P. Regnault, and C. Vettier, *J. Phys. Chem. Solids* **59**, 2135 (1998).
- [18] P. Bourges, Y. Sidis, H.F. Fong, B. Keimer, L.P. Regnault, J. Bossy, A.S. Ivanov, D.L. Milius, and I.A. Aksay, in *High Temperature Superconductivity* S.E. Barnes *et al.*, Eds. (CP483, American Institute of Physics, Amsterdam, 1999) p. 207 (cond-mat/9902067).
- [19] P. Dai, H.A. Mook, and F. Dogan, *Phys. Rev. Lett.* **80**, 1738, (1998) (cond-mat/9707112).
- [20] H.A. Mook, P. Dai, S.M. Hayden, G. Aeppli, T.G. Perring, and F. Dogan, *Nature* **395**, 580 (1998).
- [21] H.F. Fong, P. Bourges, Y. Sidis, L.P. Regnault, J. Bossy, A. Ivanov, D.L. Milius, I.A. Aksay, and B. Keimer, *Phys. Rev. Lett.*, **82** 1939 (1999).
- [22] H.F. Fong, P. Bourges, Y. Sidis, L.P. Regnault, A. Ivanov, G.D. Gu, N. Koshizuka, and B. Keimer, *Nature* **398**, 588 (1999).
- [23] See, *e.g.*, P. Gautier-Picard, E. Beaugnon, X. Chaud, A. Sulpice and R. Tournier, *Physica C* **308**, 161 (1994).
- [24] For a detailed description of the polarized beam technique, see Ref. [11], and R.M. Moon, T. Riste and W.C. Koehler, *Phys. Rev.* **181**, 920 (1969); G. Shirane in *Frontiers of Neutron Scattering*, (North-Holland, Amsterdam, 1986).
- [25] V.N.K. Zhuchenko, *J. Phys. I (France)* **7**, 177 (1997).
- [26] P. Bourges *et al.*, to be published.
- [27] I.I. Mazin and V.M. Yakovenko, *Phys. Rev. Lett.* **75**, 4134 (1995).
- [28] A.J. Millis and H. Monien, *Phys. Rev. B* **54**, 16172 (1996).
- [29] N. Bulut and D.J. Scalapino, *Phys. Rev. B* **53**, 5149 (1996).
- [30] G. Blumberg, B.P. Stojkovic, and M.V. Klein, *Phys. Rev. B* **52**, 15741 (1995).
- [31] D.L. Liu, Y. Zha and K. Levin, *Phys. Rev. Lett.* **75**, 4130 (1995).
- [32] C. Stemann, C. Pépin, and M. Lavagna, *Phys. Rev. B* **50**, 4075 (1994).
- [33] M. Lavagna and C. Stemann, *Phys. Rev. B* **49**, 4235 (1993).
- [34] F. Onufrieva and J. Rossat-Mignod, *Phys. Rev. B* **52**, 7572 (1995).
- [35] F. Onufrieva, *Physica C* **251**, 348 (1995).
- [36] F. Onufrieva and P. Pfeuty, cond-mat/9903097.
- [37] V. Barzykin and D. Pines, *Phys. Rev. B* **52** 13585 (1995).
- [38] D.K. Morr and D. Pines, *Phys. Rev. Lett.* **81**, 1086 (1998).

- [39] F.F. Assaad and M. Imada, Phys. Rev. B **58**, 1845 (1998).
- [40] E. Demler and S.C. Zhang, Phys. Rev. Lett. **75**, 4126 (1995).
- [41] S.C. Zhang, Science **275**, 1089 (1997).
- [42] E. Demler, H. Kohno, and S.C. Zhang, Phys. Rev. B **58**, 5719 (1998).
- [43] Z.Y. Weng, D.N.Sheng, C.S.Ting, Phys. Rev. Lett. **80**, 5401 (1998).
- [44] H. Yoshikawa and T. Moriya, J. Phys. Soc. Jpn. **68**, 1340 (1999).
- [45] J. Brinckmann and P.A. Lee, Phys. Rev. Lett. **82**, 2915 (1999).
- [46] A.A. Abrikosov, Phys. Rev. B **57**, 8656 (1998).
- [47] L. Yin, S. Chakravarty and P.W. Anderson, Phys. Rev. Lett. **78**, 3559 (1997).
- [48] V.J. Emery, S.A. Kivelson and O. Zachar, Phys. Rev. B **56**, 6120 (1997).
- [49] M. Greiter, Phys. Rev. Lett. **79**, 4898 (1997).
- [50] G. Baskaran and P.W. Anderson, J. Phys. Chem. Solids **59**, 1780 (1998).
- [51] See, e.g., N. Bernhoeft, N. Sato, B. Roessli, N. Aso, A. Hiess, G. H. Lander, Y. Endoh, and T. Komatsubara, Phys. Rev. Lett. **81**, 4244 (1998).
- [52] J.M. Tranquada, G. Shirane, B. Keimer, S. Shamoto and M. Sato, Phys. Rev. B **40**, 4503 (1989).
- [53] D. Reznik, P. Bourges, H.F. Fong, L.P. Regnault, J. Bossy, C. Vettier, D.L. Milius, I.A. Aksay and B. Keimer, Phys. Rev. B **53**, R14741 (1996).
- [54] S.W. Lovesey, *Theory of Neutron Scattering from Condensed Matter* (Clarendon Press, Oxford, 1984).
- [55] S.M. Hayden, G. Aeppli, H.A. Mook, T.G. Perring, T.E. Mason, S.-W. Cheong and Z. Fisk, Phys. Rev. Lett. **76**, 1344 (1996).
- [56] P. Dai, H.A. Mook, S.M. Hayden, G. Aeppli, T.G. Perring, R.D. Hunt, and F. Dogan, Science **284**, 1344 (1999).
- [57] E. Manousakis, Rev. Mod. Phys. **63**, 1 (1991), and references therein; J. Igarashi, Phys. Rev. B **46**, 10763 (1992).
- [58] P. Bourges, H. Casalta, A.S. Ivanov, and D. Petitgrand Phys. Rev. Lett. **79**, 4906 (1997).
- [59] R.J. Cava, A.W. Hewat, E.A. Hewat, B. Batlogg, M. Marezio, K.M. Rabe, J.J. Krajewski, W.F. Peck, and L.W. Rupp, Physica C **165**, 419 (1990).
- [60] W. Reichardt, J. of Low Temp. Phys., **105**, 807 (1996). L. Pintschovius, and W. Reichardt, in *Neutron Scattering in Layered Copper-Oxide Superconductors*, Edited by A. Furrer, 165 (Kluwer, Amsterdam, 1998).
- [61] M. Arai, T. Nishijima, Y. Endoh, T. Egami, S. Tajima, K. Tomimoto, Y. Shiohara, M. Takahashi, A. Garret, and S.M. Bennington, Phys. Rev. Lett. **83**, 608 (1999).
- [62] A.V. Balatsky, and P. Bourges, Phys. Rev. Lett. **82**, 5337 (1999).
- [63] K. Yamada, S. Wakimoto, G. Shirane, C.H. Lee, M.A. Kastner, S. Hosoya, M. Greven, Y. Endoh, and R.J. Birgeneau, Phys. Rev. Lett. **75**, 1626 (1995).
- [64] B. Lake, G. Aeppli, T. E. Mason, A. Schroder, D. F. McMorrow, K. Lefmann, M. Isshiki, M. Nohara, H. Takagi, and S. M. Hayden, Nature **400**, 43 (1999).
- [65] K. Kakurai, S. Shamoto, T. Kiyokura, M. Sato, J.M. Tranquada, and G. Shirane, Phys. Rev. B **48**, 3485 (1993).
- [66] Y. Sidis, P. Bourges., B. Hennion, L.P. Regnault, R. Villeneuve, G. Collin, and J.F. Marucco, Phys. Rev. B **53**, 6811 (1996).
- [67] See, e.g., H. Yasuoka, S. Kambe, Y. Itoh, and T. Machi, Physica B **199**, 278 (1994).
- [68] See, e.g., C. Berthier, M.H. Julien, M. Horvatic, and Y. Berthier, J. Phys. I (France) **6**, 2205 (1997).
- [69] See, e.g., D.J. van Harlingen, Rev. Mod. Phys. **67**, 515 (1995).
- [70] D.M. King, Z.X. Shen, D.S. Dessau, D.S. Marshall, C.H. Park, W.E. Spicer, J.L. Peng, Z.Y. Li, and R.L. Greene, Phys. Rev. Lett. **73**, 3298 (1994).
- [71] J.M. Harris, Z.X. Shen, P.J. White, D.S. Marshall, M.C. Schable, J.N. Eckstein, and I. Bozovic, Phys. Rev. B **54**, 15665 (1996).
- [72] D.J. Scalapino and S.R. White, Phys. Rev. B **58** 8222 (1998).
- [73] E. Demler and S.C. Zhang, Nature **396**, 733 (1998).
- [74] S. Chakravarty and H.K. Kee, cond-mat/9908205.
- [75] J.M. Tranquada, Physica C **282**, 166 (1997).
- [76] See, e.g., H. Fukuyama, Physica C **263**, 35 (1996).
- [77] J.W. Loram, K.A. Mirza, J.R. Cooper, and W.Y. Liang, Phys. Rev. Lett. **71**, 1740 (1993).
- [78] M.R. Norman, H. Ding, J.C. Campuzano, T. Takeuchi, M. Randeria, T. Yokoya, and T. Takahashi, Phys. Rev. Lett. **79**, 3506 (1997).
- [79] A. Abanov and A.V. Chubukov, Phys. Rev. Lett. **83**, 1652 (1999).
- [80] A very good and well documented FFT implementation in C can be obtained from <http://theory.lcs.mit.edu/~fft/>.

FIG. 1.  $T_c$  curve of the  $\text{YBa}_2\text{Cu}_3\text{O}_{6.7}$  sample using the depolarization technique as described in the text. The spectrometer is set for the (006) nuclear Bragg reflection. The flipping ratio, defined as the ratio of neutrons scattered without spin flip to those that are scattered with a spin flip, is infinite at a nuclear Bragg reflection in an ideal setup, but finite (here: 16) because of incomplete beam polarization. With the sample field cooled into the superconducting state and then rotated by  $90^\circ$ , the flipping ratio is reduced by trapped flux.

FIG. 2. A scan of even channel excitations at 55 meV that exemplifies the usefulness of numerical simulations of the lattice dynamics. The dotted line, derived from the phonon simulation program described in the text, provides a good description of the background features. The peak in the center is magnetic. The solid line is a guide-to-the-eye.

FIG. 3. Typical constant-energy scans taken on the  $\text{YBa}_2\text{Cu}_3\text{O}_{6.5}$  sample in the odd channel. The solid lines are the results of fits to Gaussian profiles. The energies of the data in the three panels are evenly spaced (50 meV, 65 meV, and 80 meV). The dotted lines that join the split peaks go through ( $H = 0.5\text{r.l.u.}$ ,  $E = 0\text{meV}$ ) and illustrate a spin-wave-like dispersion, as described in the text.

FIG. 4. Typical constant-energy scans obtained on the  $\text{YBa}_2\text{Cu}_3\text{O}_{6.7}$  sample, in (a) odd and (b) even excitation channels. The top panel of (b) shows ILL data, the rest are from LLB experiments. The lines are the results of fits to Gaussian profiles.

FIG. 5. Local (2D wave vector averaged) susceptibility of  $\text{YBa}_2\text{Cu}_3\text{O}_{6.5}$  in the (a) odd and (b) even excitation channels, obtained by fitting constant-energy scans. Solid lines are guides-to-the-eye. The dotted line indicates the low-energy local susceptibility of the 2D Heisenberg antiferromagnet (Eq. 6).

FIG. 6. Local (2D wave vector averaged) susceptibility of  $\text{YBa}_2\text{Cu}_3\text{O}_{6.7}$  in the (a) odd and (b) even excitation channels. Solid lines are guides-to-the-eye. The dashed line superposed on the top (12 K) spectrum reproduces the solid line for the 70K data and illustrates the effect of entering the superconducting state. The dotted line indicates the low-energy local susceptibility of the 2D Heisenberg antiferromagnet (Eq. 6) (from [15]).

FIG. 7. Same data as in Fig. 6, but showing the intensity at  $\mathbf{Q}_0 = (\pi, \pi)$  instead of the local susceptibility.

FIG. 8. Temperature dependence of the local susceptibility at the energies at which the magnetic resonance occurs in both underdoped samples. Superconducting critical temperatures are marked with arrows. The solid symbols are obtained using polarized neutron scattering techniques.

FIG. 9. Difference of (a) the susceptibility  $\chi''(\mathbf{Q}_0, \omega)$  and (b) the spin-spin correlation function,  $S(\mathbf{Q}_0, \omega)$  in the superconducting and normal states, for  $\text{YBa}_2\text{Cu}_3\text{O}_{6.5}$ . Normal state data are taken at 60 K, just above  $T_c = 52$  K.

FIG. 10. Difference of (a) the susceptibility  $\chi''(\mathbf{Q}_0, \omega)$  and (b) the spin-spin correlation function,  $S(\mathbf{Q}_0, \omega)$  in the superconducting and normal states, for  $\text{YBa}_2\text{Cu}_3\text{O}_{6.7}$ . Normal state data are taken at 80 K, just above  $T_c = 67$  K. The open circles represent data taken at BNL, the filled circles are data taken at LLB.

FIG. 11. A synopsis of (a) the superconducting transition temperature, (b) the energy-integrated spectral weight evaluated at  $\mathbf{Q}_0 = (\pi, \pi)$ , and (c) of the energy of the magnetic resonance peak in the two underdoped samples, compared to those of the optimally doped sample with  $T_c = 93$  K. Horizontal error bars indicate a conservative confidence level for the oxygen content.

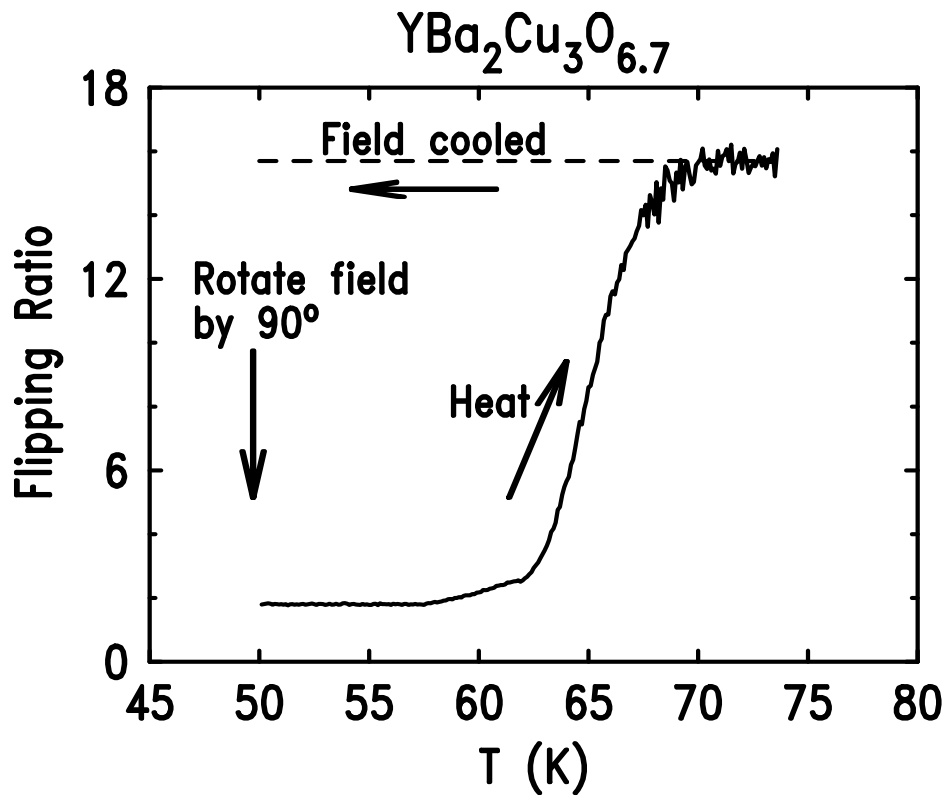
FIG. 12. Typical constant-energy scan at 24 meV taken with polarized neutrons in the spin-flip channel on  $\text{YBa}_2\text{Cu}_3\text{O}_{6.7}$  in (a) the superconducting and (b) the normal state. Open circles are horizontal field (HF) measurements taken after the sample was field cooled with the field parallel to the scattering vector. Solid circles are measurements taken after the sample was cooled in vertical field (VF), perpendicular to the scattering plane. For magnetic scattering, the background-corrected HF intensity should be twice the VF intensity because of polarization factors in the magnetic neutron cross section (Eq. 10). The solid lines indicate that this is indeed the case.

FIG. 13. Determination of the spin gap in  $\text{YBa}_2\text{Cu}_3\text{O}_{6.7}$  by polarized neutrons. The lines are guides-to-the-eye. Open square symbols are from direct subtraction between HF and VF intensity as in the previous figure. Solid square symbols are HF polarized beam background from curve fitting such data. Open circles are the amplitudes resulting from these fits. Note that the scales on left and right vertical axis are the same.

FIG. 14. Local susceptibility at 65 meV in  $\text{YBa}_2\text{Cu}_3\text{O}_{6.7}$  in both channels, showing their different temperature dependences. Note the absence of any anomaly at  $T_c$ . Lines are guides-to-the-eye.

FIG. 15. Schematic diagram summarizing the temperature evolution of the magnetic excitation spectra of the underdoped  $\text{YBa}_2\text{Cu}_3\text{O}_{6+x}$  compounds (a) in the normal state, and (b) across the superconducting transition. The even excitations evolve smoothly with temperature, parallel to (a). The odd channel excitations undergo an abrupt sharpening at the resonance energy across  $T_c$ .

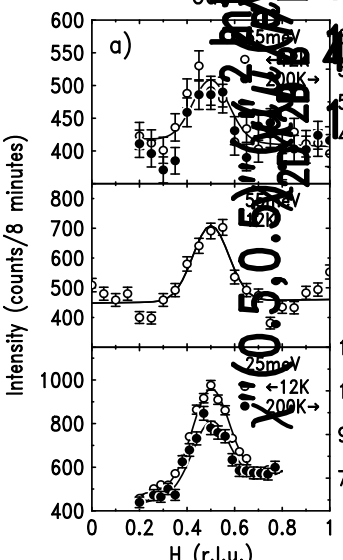
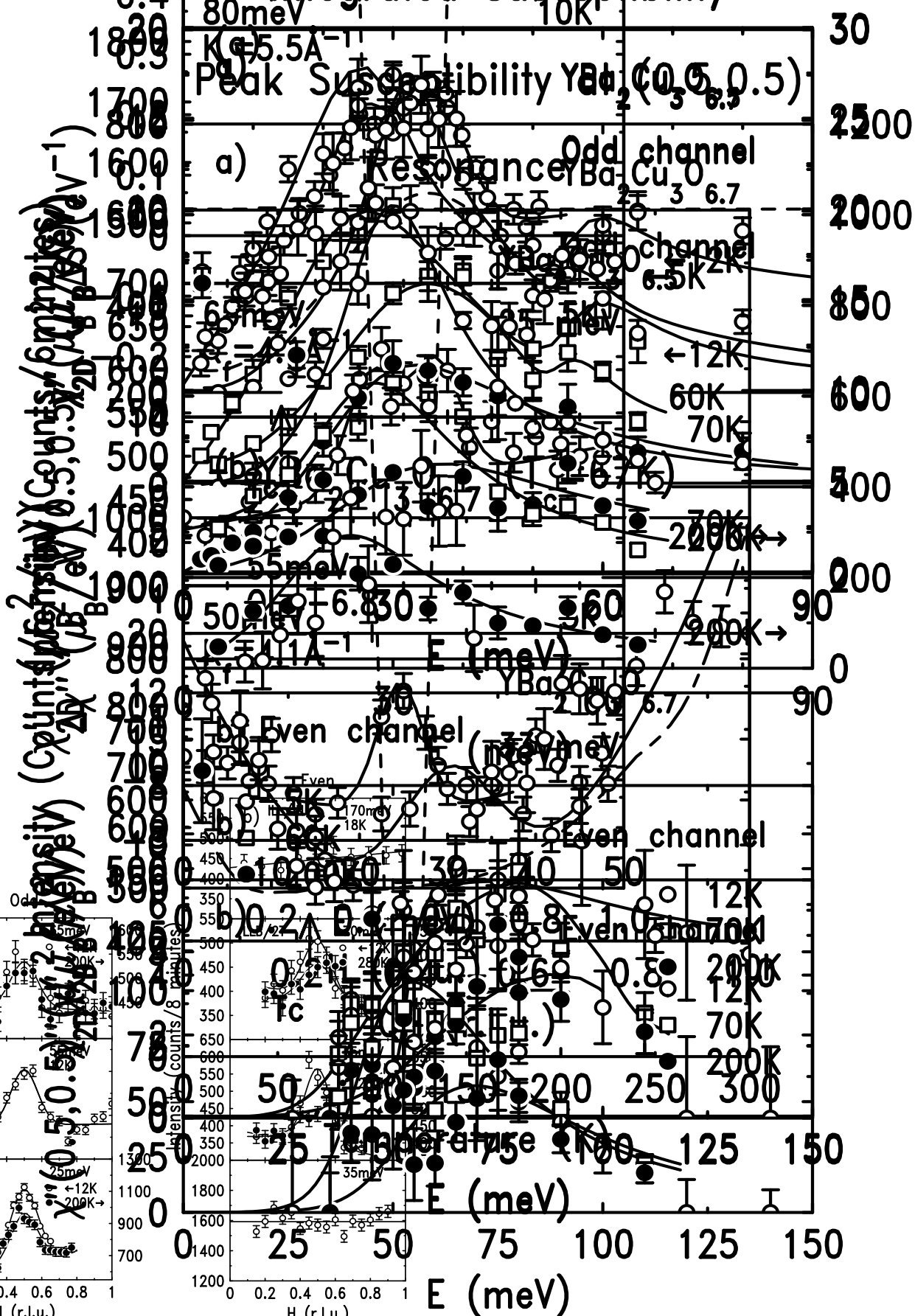
FIG. 16. Overall momentum width of the magnetic response in  $\text{YBa}_2\text{Cu}_3\text{O}_{6.7}$ , obtained as described in the text (Section V C). Particular attention was paid to the constant-energy profile at 24 meV, where an incommensurate response was identified as first observed by Dai et al. [19]. Note the pronounced broadening above 50 meV.

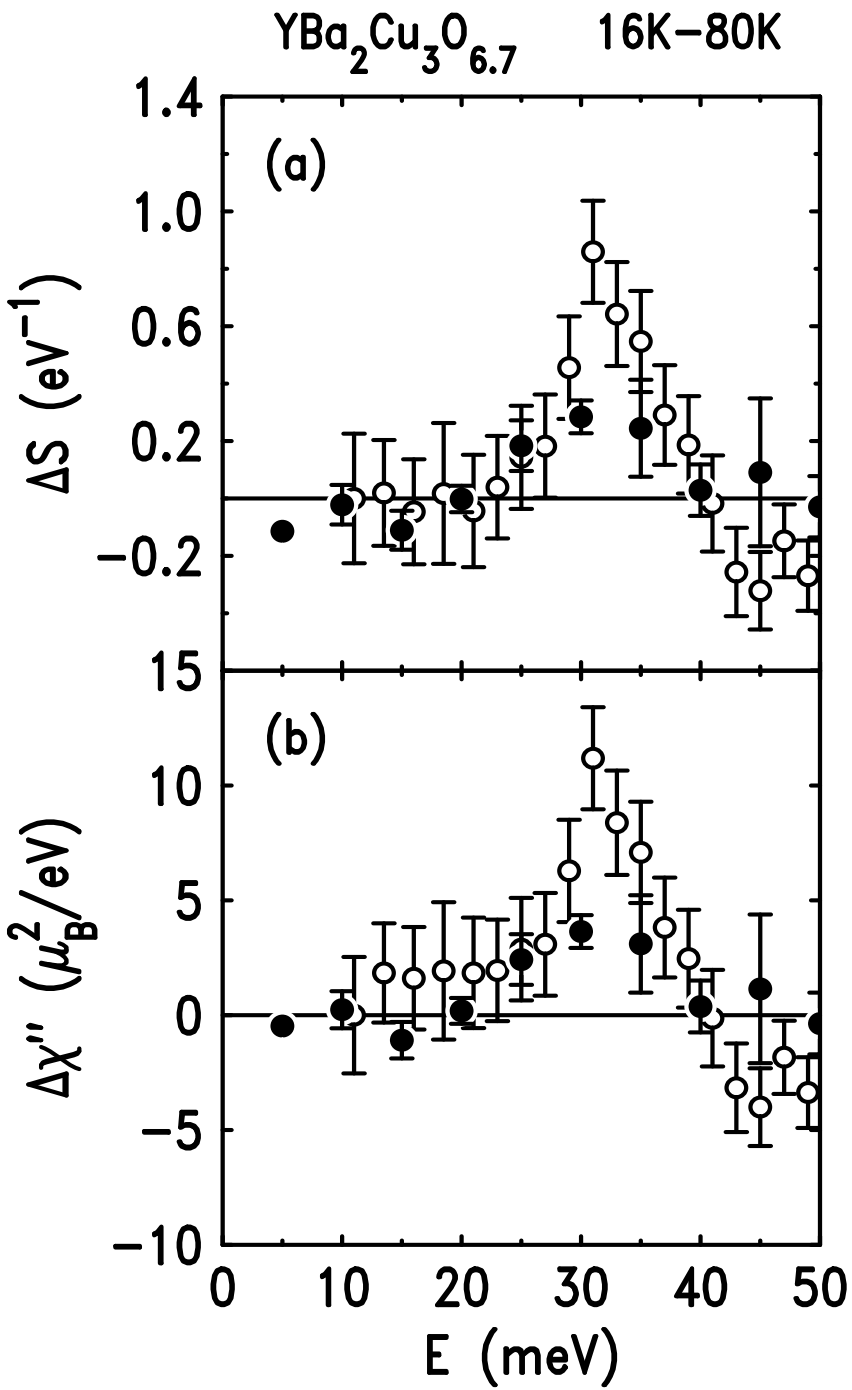


YBa<sub>2</sub>Cu<sub>3</sub>O<sub>6.5</sub> 16K-60K

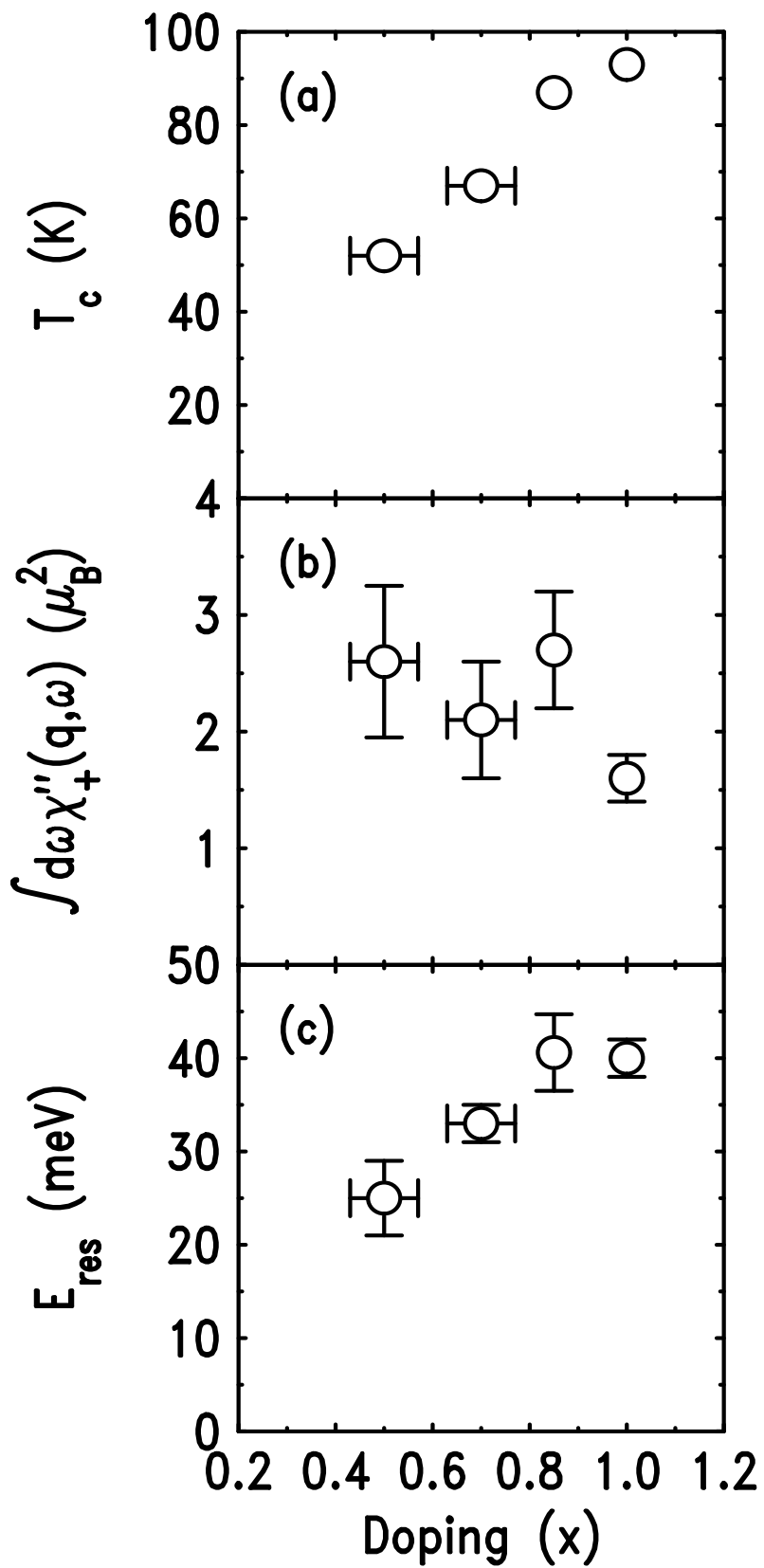
Tue Jul 6 20:09 1999

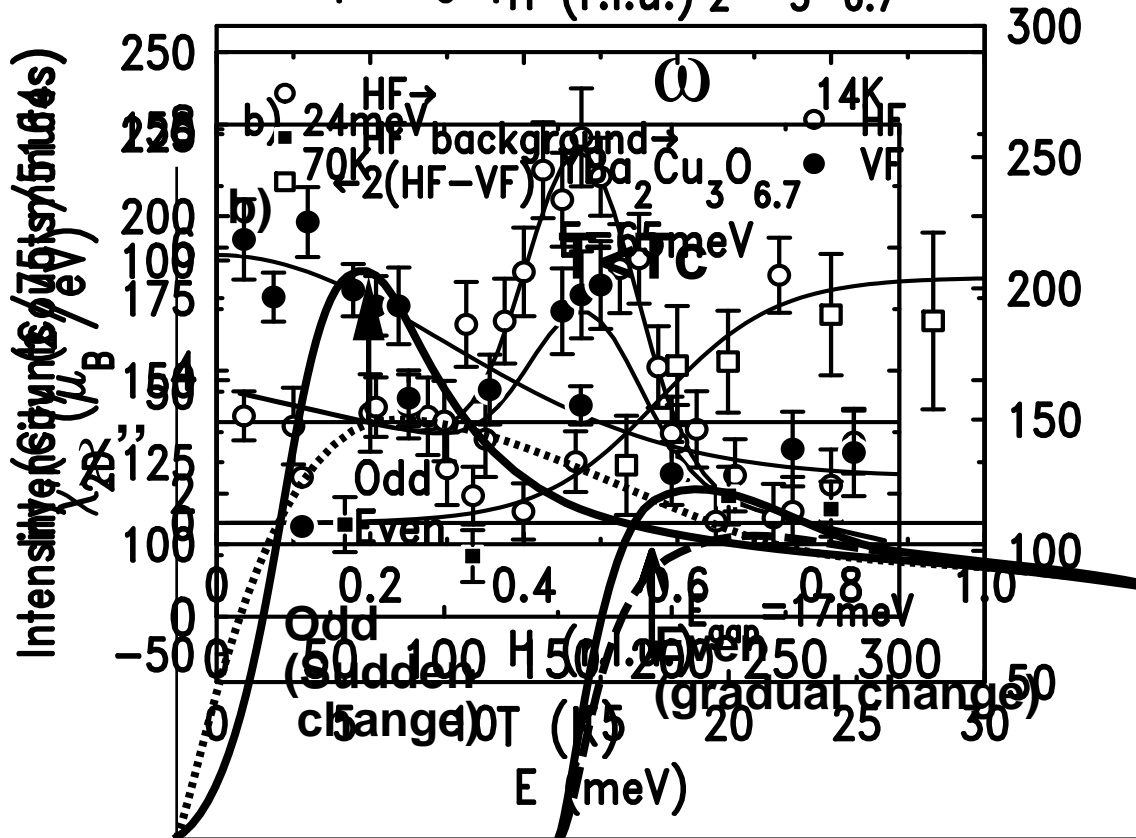
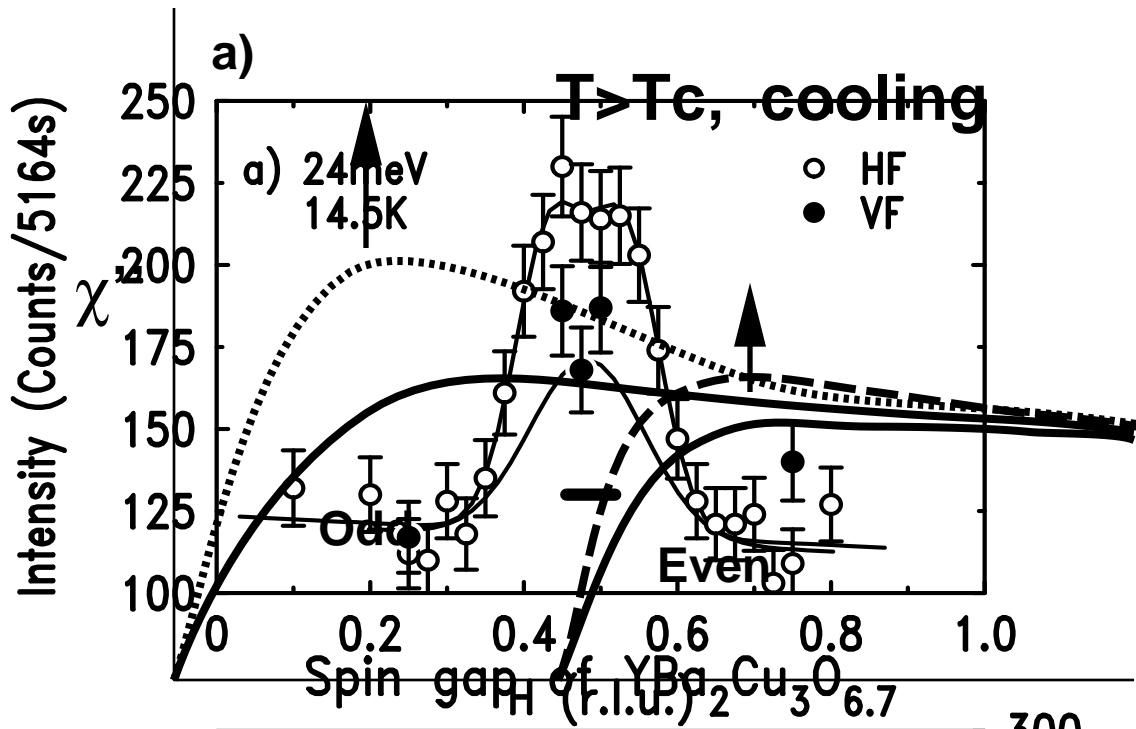
# Integrated Susceptibility











①

